TOOLING

Process stability of a novel roughing-finishing end mill

B. Denkena[1] · R. Grabowski[1,2] · A. Krödel[1] · L. Ellersiek[1]

Abstract

In this paper, stability investigations of a novel roughing-finishing end mill are carried out. This tool possesses two sharp finishing teeth and two radially recessed, chamfered roughing teeth. By applying the same tool for roughing and finishing operations, tool changes and process time can be reduced. For the stability investigations, the semi-discretization method for calculating stability charts was extended and made applicable for the novel tool concept by taking into account the radial recession of the chamfered cutting teeth. This is necessary because the radial recession leads to varying time-delays during the tooth engagement. Stability charts were then calculated for roughing-finishing tools with different radial recession as well as for conventional finishing and roughing tools. Furthermore, experimental stability charts were created. The results show a good agreement between calculated and experimental stability charts for the finishing tool. However, the calculated stability limits of the roughing-finishing tool and the roughing tool do not met with the experimental stability limits, which is attributed to inaccuracies in the modelling of process damping. Nevertheless, calculated as well as experimental stability charts indicate a significant increase of the stability limit of the roughing-finishing tool compared to the finishing tool.

Keywords Process stability · Process damping · Roughing · Finishing · Semi-discretization

1 Introduction

In high performance cutting, the machining processes aim for high material removal rates. Besides the power limit of the machine tool, chatter vibrations are of high importance regarding a high productivity. Chatter vibrations can mostly be attributed to the regenerative effect [1, 2]. This effect is based on the assumption that a cutting tooth does not generate an ideal smooth surface. Instead, a defined waviness on the surface is created due to the dynamic compliance of the system. Therefore, the following tooth has to cut the wavy surface, the so-called outer modulation. In addition to this, the tooth vibrates with a phase shift ε to the outer modulation. This vibration path is called inner modulation. Therefore, the phase shift ε leads to a dynamic uncut chip thickness. In case of regenerative chatter, the vibrations of the individual tooth increase due to the dynamic uncut chip

thickness and result in an unstable system. This effect is pictured in Fig. 1.

Since a higher depth of cut increases the dynamic forces of the regenerative effect, cutting processes are mostly stable to a certain depth of cut, the so-called stability limit, and unstable for higher depth of cut. To increase the stability limit of cutting processes, various methods can be used. One of the most common methods is the disturbance of the regenerative effect through varying time delays [4]. This can be achieved for example by serrated cutting edges [5], varying helix angles [6] or spindle speed variation techniques [7]. Another mechanism leading to higher stability limits is the process damping effect. When a cutting tooth penetrates the material, for example due to material springback or periodic vibrations, a force arises as a result of the elastic deformation of the material. This force can be modelled as product of indented volume V, friction coefficient μ and a constant K_{pd} (Eq. 1).

$$
\begin{aligned}
F_{r,pd}\langle t \rangle &= V\langle t \rangle K_{pd} \\
F_{t,pd}\langle t \rangle &= \mu V\langle t \rangle K_{pd}
\end{aligned}
\tag{1}
$$

The model was first derived by Wu [8] and thereafter adapted by various other authors [9–13]. In literature, the consideration of process-damping effects has taken place mostly for worn tools [11, 13]. However, a significant increase due to

✉ L. Ellersiek
   ellersiek@ifw.uni-hannover.de

1 Institute of Production Engineering and Machine Tools, Leibniz Universität Hannover, Hanover, Germany

2 IAV GmbH, Gifhorn, Germany
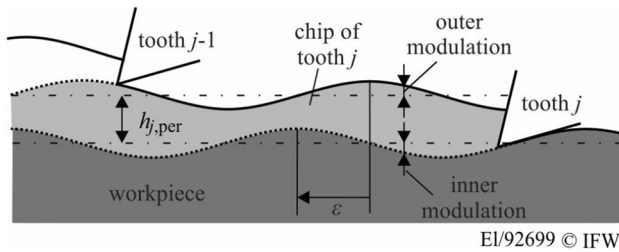
Fig. 1 Inner and outer modulation [3]

the process damping effect can also be achieved with flank face chamfers [3]. The disadvantages of chamfered cutting teeth are burr formation and a higher surface roughness compared to tools with only sharp cutting teeth [14]. Therefore, an additional finishing process has to be carried out, leading to higher process times. In this paper, a novel tool concept, which is applicable for roughing as well as finishing operations, is examined [15, 16]. Thereby, the number of tool changes can be reduced. The tool possesses two chamfered, radial recessed cutting teeth and two sharp cutting teeth. Due to the radial recession ΔR, the chamfered cutting teeth do not get in contact with the final surface. Thus, surface defects from the chamfered cutting tooth are always cut off by the following sharp tooth. Moreover, the radial recession ΔR leads to a higher maximum uncut chip thickness on the finishing teeth. In order to compensate the resulting higher thermomechanical loads, the tool is unequally pitched. To avoid a contact between chamfer and workpiece due to runout errors or tool wear, ΔR should be greater than 10 μm. Nevertheless, it is expected that a higher tool wear arises for the chamfered teeth, and ΔR therefore increases with increasing wear. The tool concept is pictured in Fig. 2.

Investigations of the achieved surface quality with the roughing-finishing tool were carried out and discussed in [15, 17]. Compared to a conventional roughing tool, a significant reduction of burr formation and the avoidance of material adhesions on the workpiece surface could be detected. Furthermore, a higher dimensional accuracy could be achieved due to lower tool deflection and surface generating forces [15].

The objective of this paper is the investigation of the process stability of the roughing-finishing tool concept. Therefore, the semi-discretization method for calculating stability charts was extended. With this method, the influence of different tool geometries on the process stability can be investigated without extensive cutting experiments. Moreover, experimental stability charts were created for two roughing-finishing tools with different radial recession ΔR, one conventional roughing tool with only chamfered cutting teeth and one conventional finishing tool with only sharp cutting teeth. Furthermore, stability charts were calculated with the semi-discretization method and the input parameters derived. The results are presented and discussed.
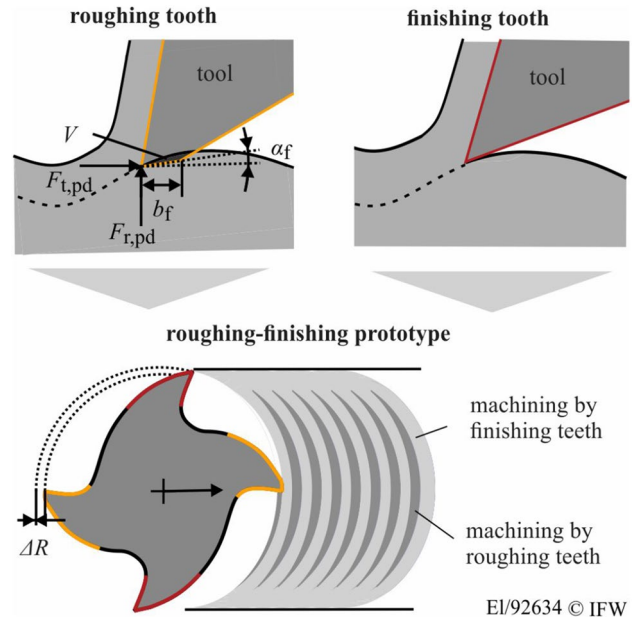
Fig. 2 Roughing-finishing tool concept

2 Modelling of the dynamic behaviour

In this paper, the process stability was determined using the semi-discretization method derived in [3, 15]. The method is described briefly in the following. In general, the dynamics of the milling process can be expressed by Eq. (2). The left hand side of the equation describes the dynamics of the system, while the right hand side depicts the force resulting from the uncut chip thickness.

$$M\ddot{q}\langle t\rangle + D\dot{q}\langle t\rangle + Kq\langle t\rangle = T_q^{\mathrm{T}} \sum_{j=1}^{N_t} Q_j\langle t\rangle (\Delta q\langle t - \theta_j\rangle - \Delta q\langle t\rangle) \tag{2}$$

N_{t} is the number of teeth. θ_{j} describes the time between two tooth engagements. The matrices M, D and K contain mass, damping and stiffness of the single modes of tool and workpiece in x- and y-direction. The individual frequency response functions are modelled as superposition of single modes. The total displacement, as pictured in Fig. 3a, can be calculated as superposition of the displacement of the single modes (Eq. (3)).

$$x_{\mathrm{w}}\langle t\rangle = \sum_{i=1}^{r} x_{\mathrm{w},i}\langle t\rangle \quad y_{\mathrm{w}}\langle t\rangle = \sum_{i=1}^{s} y_{\mathrm{w},i}\langle t\rangle$$

$$x_t\langle t\rangle = \sum_{i=1}^{u} x_{t,i}\langle t\rangle \qquad y_t\langle t\rangle = \sum_{i=1}^{v} y_{t,i}\langle t\rangle \tag{3}$$

$$w = r + s + u + v$$
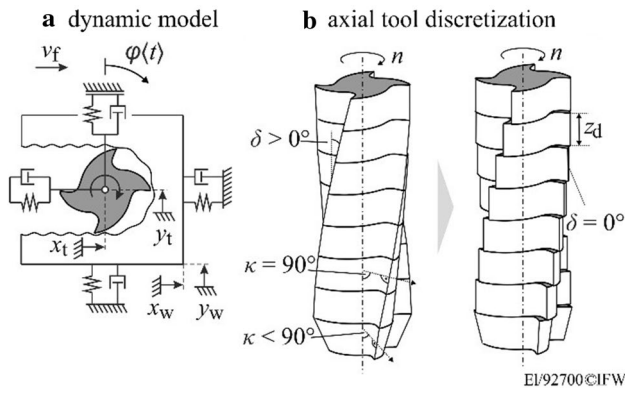
Fig. 3 a Dynamic model of the milling process [3]. **b** Axial tool discretization [15]

The terms r, s, u and v are the number of modes in x- and y-direction for workpiece and tool. The vector $q\langle t\rangle$ describes the dynamic deflection of each single mode. By multiplying $q\langle t\rangle$ with the matrix T_q, the vector $\Delta q\langle t\rangle$ can be calculated, which contains the relative dynamic displacement in x- and y-direction between tool and workpiece. Therefore, $\Delta q\langle t-\theta_j\rangle$ is the outer modulation and $\Delta q\langle t\rangle$ the inner modulation. T_q is defined as

$$T_q = \begin{bmatrix} 1_{(1,r)} & 0 & -1_{(1,u)} & 0 \\ 0 & 1_{(1,s)} & 0 & -1_{(1,v)} \end{bmatrix} \quad (4)$$

By applying Eq. (2) on the roughing-finishing tool, certain extensions have to be made. To consider the influence of the chamfer, a velocity-dependant process damping term has to be added [3]. Furthermore, the individual cutting teeth possess different radii. Therefore, the time-delay term can be time-dependant and it has to be taken into account, which tooth was in cut previously. Moreover, the varying process forces along the end mill axis are considered by dividing the z-axis in N_z discrete segments with length z_d and helix angle $\delta = 0°$ for the individual segments (Fig. 3b).

These extensions result in the following second-order linear delay differential equation:

$$M\ddot{q}\langle t\rangle + Q_d\dot{q}\langle t\rangle + Q_k q\langle t\rangle$$
$$= T_q^T \sum_{j,u=1}^{N_t} \sum_{i=1}^{N_z} Q_{j,u}\langle t,z_i\rangle \Delta q\langle t - \theta_{j,u}\langle z_i\rangle\rangle$$

with

$$Q_k\langle t\rangle = K + T_q^T \sum_{j,u=1}^{N_t} \sum_{i=1}^{N_z} Q_{j,u}\langle t,z_i\rangle T_q \quad (5)$$

$$Q_d\langle t\rangle = D + T_q^T \sum_{j,u=1}^{N_t} \sum_{i=1}^{N_z} Q_{pd,j,u}\langle t,z_i\rangle T_q$$

The matrix $Q_{j,u}\langle t\rangle$ contains the projected cutting force coefficients according to Eq. (6). Thereby, $g_{j,u}\langle t\rangle$ is a step-function, which is 1, if the j-th tooth is in cut with u as previous tooth and 0 else. K_{tc} and K_{rc} are tangential and radial cutting force coefficients, respectively.

$$Q_{j,u}\langle t,z_i\rangle = T_{j,dyn}\langle t,z_i\rangle \begin{bmatrix} 0 & K_{tc} \\ 0 & K_{rc} \end{bmatrix} T_{j,dyn}^{-1}\langle t,z_i\rangle z_d g_{j,u}\langle t,z_i\rangle$$

with

$$T_{j,dyn}\langle t,z_i\rangle = \begin{bmatrix} cos(-\varphi_j\langle t,z_i\rangle) & -sin(-\varphi_j\langle t,z_i\rangle)sin(\kappa_j\langle z_i\rangle) \\ sin(-\varphi_j\langle t,z_i\rangle) & cos(-\varphi_j\langle t,z_i\rangle)sin(\kappa_j\langle z_i\rangle) \end{bmatrix}$$
$$(6)$$

The matrix $Q_{pd},j,u\langle t,z_i\rangle$ describes the process damping force and is defined as follows:

$$Q_{pd,j,u}\langle t,z_i\rangle$$
$$= \frac{b_f^2}{2v_c} T_{j,dyn}\langle t,z_i\rangle \begin{bmatrix} 0 & 1 \\ 0 & \mu \end{bmatrix} K_{pd} T_{j,dyn}^{-1}\langle t,z_i\rangle z_d g_{j,u}\langle t,z_i\rangle \quad (7)$$

The second order differential Eq. (5) can be transformed into the first order differential Eq. (8).

$$\dot{x}\langle t\rangle = A\langle t\rangle x\langle t\rangle + \sum_{j,u=1}^{N_t} \sum_{i=1}^{N_z} B_{j,u}\langle t,z_i\rangle \Delta q\langle t - \theta_{j,u}\langle z_i\rangle\rangle$$

with

$$x\langle t\rangle = \begin{bmatrix} q\langle t\rangle \\ \dot{q}\langle t\rangle \end{bmatrix}$$
$$(8)$$
$$A\langle t\rangle = \begin{bmatrix} 0_{(w,w)} & I_{(w,w)} \\ M^{-1}Q_k\langle t\rangle & M^{-1}Q_d\langle t\rangle \end{bmatrix}$$
$$B\langle t\rangle = \begin{bmatrix} 0_{(w,2)} \\ M^{-1}T_q^T Q_{j,u}\langle t,z_i\rangle \end{bmatrix}$$

Thereby, I is the identity matrix. By introducing the time discrete term

$$t_d = dT + T \quad \text{with} \quad \{d \in \mathbb{N} \mid d > 0\}, \quad (9)$$

Equation (8) can be solved for a known initial state t_{d-1} for the time t_d as

$$x\langle t_d\rangle = e^{A_d(t_d-t_{d-1})} x\langle t_{d-1}\rangle$$
$$+ \sum_{j,u=1}^{N_t} \sum_{i=1}^{N_z} \int_{t_{d-1}}^{t_d} e^{A_d(t_d-\tau)} B_{d,j,u}\langle z_i\rangle \Delta q\langle \tau - \theta_{j,u}\langle z_i\rangle\rangle d\tau$$

with

$$A_d = \frac{1}{T} \int_{t_d}^{t_{d+1}} A\langle t\rangle dt$$
$$B_{d,j,u}\langle z_i\rangle = \frac{1}{T} \int_{t_d}^{t_{d+1}} B_{j,u}\langle t,z_i\rangle dt.$$
$$(10)$$

In the later calculation, one tool revolution will be discretised in N_k steps of the length T. The relative dynamic displacement $\Delta q \langle t \rangle$ in Eq. (10) can be solved iteratively for the following time step. However, with this method the integrated function $\Delta q \langle t\text{-}\theta_{j,u} \rangle \langle z_i \rangle \rangle$ is only known for discrete time-steps. The time delay term is therefore approximated by

$$(m_{j,u}\langle z_i \rangle - \gamma_{j,u}\langle z_i \rangle)T = \theta_{j,u}\langle z_i \rangle$$

with

$$\{m_{j,u}\langle z_i \rangle \in \mathbb{N} \quad | \ m_{j,u}\langle z_i \rangle \geq 1\}$$
$$\{\gamma_{j,u}\langle z_i \rangle \in \mathbb{R} \quad | \ 0 \leq \gamma_{j,u}\langle z_i \rangle < 1\}. \tag{11}$$

By assuming that $\theta_{j,u}\langle z_i \rangle \gg T$, the following case analysis

$$\tau - \theta_{j,u}\langle z_i \rangle$$
$$= \begin{cases} dT - m_{j,u}\langle z_i \rangle T & \text{if } dT \leq \tau < dT + (1 - \gamma_{j,u}\langle z_i \rangle)T \\ dT - (m_{j,u}\langle z_i \rangle - 1)T & \text{if } dT + (1 - \gamma_{j,u}\langle z_i \rangle T) \leq \tau \leq dT + T \end{cases} \tag{12}$$

can be made. This approximation is pictured in Fig. 4 for a one-dimensional case. Implementing the case analysis into Eq. (10) leads to Eq. (13):

$$x\langle dT + T \rangle = e^{A_d T}x\langle dT \rangle$$
$$+ \sum_{j,u=1}^{N_t} \sum_{i=1}^{N_z} \left[\int_{dT}^{a_0} e^{A_d(dT+T-\tau)}B_{d,j,u}\langle z_i \rangle d\tau \Delta q\langle dT - m_{j,u}\langle z_i \rangle T \rangle \right.$$
$$\left. + \int_{a_0}^{dT+T} e^{A_d(dT+T-\tau)}B_{d,j,u}\langle z_i \rangle d\tau \Delta q\langle dT - (m_{j,u}\langle z_i \rangle - 1)T \rangle \right]$$

with

$$a_0 = dT + (1 - \gamma_{j,u}\langle z_i \rangle)T \tag{13}$$

By using the substitution

$$v\langle \tau \rangle = dT + T - \tau \Rightarrow \frac{dv\langle \tau \rangle}{d\tau} = -1 \Leftrightarrow d\tau = -dv, \tag{14}$$
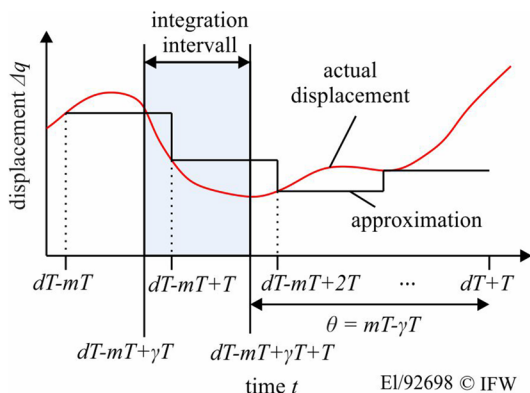
the integration limits can be adjusted as

$$x\langle dT + T \rangle = e^{A_d T}x\langle dT \rangle$$
$$+ \sum_{j,u=1}^{N_t} \sum_{i=1}^{N_z} \left[\int_{\gamma_{j,u}\langle z_i \rangle T}^{T} e^{A_d v}B_{d,j,u}\langle z_i \rangle dv \Delta q\langle dT - m_{j,u}\langle z_i \rangle T \rangle \right.$$
$$\left. + \int_{0}^{\gamma_{j,u}\langle z_i \rangle T} e^{A_d v}B_{d,j,u}\langle z_i \rangle dv \Delta q\langle dT - (m_{j,u}\langle z_i \rangle - 1)T \rangle \right]. \tag{15}$$

Equation (15) can be summarized as

$$x\langle dT + T \rangle = \Phi_d\langle T \rangle x\langle dT \rangle$$
$$+ \sum_{j,u=1}^{N_t} \sum_{i=1}^{N_z} [\Gamma_{d,j,u,1}\langle T, z_i \rangle \Delta q\langle dT - m_{j,u}\langle z_i \rangle T \rangle$$
$$+ \Gamma_{d,j,u,2}\langle T, z_i \rangle \Delta q\langle dT - (m_{j,u}\langle z_i \rangle - 1)T \rangle] \tag{16}$$

with

$$\Phi_d\langle t \rangle = e^{A_d t}$$
$$\Gamma_{d,j,u,1}\langle T, z_i \rangle = \Gamma_{d,j,u}\langle T, z_i \rangle - \Gamma_{d,j,u}\langle \gamma_{j,u}\langle z_i \rangle T, z_i \rangle$$
$$\Gamma_{d,j,u,2}\langle T, z_i \rangle = \Gamma_{d,j,u}\langle \gamma_{j,u}\langle z_i \rangle T, z_i \rangle.$$

Thereby $\Gamma_{d,j,u}$ is defined as

$$\Gamma_{d,j,u}\langle T, z_i \rangle = \int_{0}^{t} e^{A_d v}B_{d,j,u}\langle z_i \rangle dv$$
$$= A_d^{-1}(e^{A_d t} - I_{(2w,2w)})B_{d,j,u}\langle z_i \rangle. \tag{17}$$

By expanding the vector $x\langle T \rangle$ to

$$x_{exp}\langle dT \rangle = \begin{bmatrix} x\langle dT \rangle \\ \Delta q\langle dT - T \rangle \\ \Delta q\langle dT - 2T \rangle \\ \vdots \\ \Delta q\langle dT - mT \rangle \end{bmatrix} \tag{18}$$

with

$$m = \max(m_{j,u}\langle z_i \rangle)$$

the system can be expressed as

$$x_{exp}\langle dT + T \rangle = \Phi_{exp,d}\langle T \rangle x_{exp}\langle dT \rangle \tag{19}$$

where $\Phi_{exp,d}\langle T \rangle$ is the monodromy matrix. The construction of the matrix is shown in Fig. 5.

For the stability analysis, the monodromy matrix has to be calculated for a whole system period T_{per}. For equal tooth pitch and cutting edge radii, T_{per} equals mT. If tool runout is considered, T_{per} corresponds to one tool revolution. According to the Floquet theorem, the monodromy matrix of a system period can be calculated as

Fig. 4 Discrete approximation of the relative displacement Δq

$$x_{\exp}\langle T + T_{\text{per}}\rangle = \mathbf{\Phi}_{\exp,\text{per}}\langle T\rangle x_{\exp}\langle dT\rangle$$

with

$$T_{\text{per}} = pT, \quad \mathbf{\Phi}_{\exp,\text{per}}\langle T\rangle = \prod_{d=1}^{p} \mathbf{\Phi}_{\exp,d}\langle T\rangle. \tag{20}$$

To determine the stability of the system, an eigenvalue analysis has to be conducted:

$$eig(\mathbf{\Phi}_{\exp,\text{per}}\langle T\rangle) \begin{cases} < 1, & \text{stable} \\ = 1, & \text{stability limit} \\ > 1, & \text{unstable} \end{cases} \tag{21}$$

To calculate stability charts, the eigenvalue analysis has to be conducted for various combinations of spindle speed n and depth of cut a_{p}.

3 Experimental setup

3.1 Cutting experiments

Besides the mathematical examination of the process stability, the process stability was determinated experimentally on a Heller MC16 machine tool for machining of Al7075. The experimental setup is shown in Fig. 6. A unidirectional flexure was used to provoke chatter vibrations and prevent damage of the machine tool. To exclude influences of the minor cutting edge, the experiments were conducted with free corner radius. Therefore, the workpieces were prepared for the specific depths of cut a_{p}. The results of the modal analysis suggest that the preparation does not have a significant influence on the dynamic behaviour.
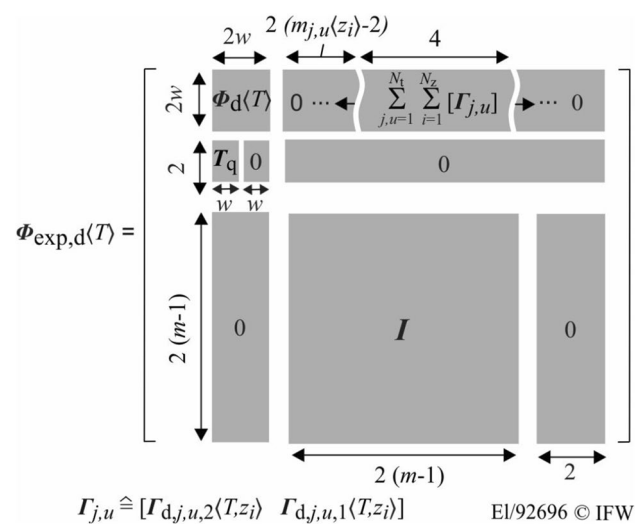
The experiments were conducted with two novel roughing-finishing prototypes ($\Delta R = 40$ µm and 20 µm), a conventional finishing tool with only sharp cutting teeth and a conventional roughing tool with only chamfered cutting teeth. All tools possess four teeth and an unequal pitch angle $\Delta p = 10°$. The chamfers have a chamfer width $b_{\text{f}} = 200$ µm and a chamfer angle $\alpha_{\text{f}} = 1°$. Stability charts were created for spindle speeds $n = 2000–10,000$ min^{-1}, a feed per tooth $f_{\text{z}} = 0.12$ mm and full radial immersion. The process stability was evaluated based on the force signal, noise emissions and chatter marks. To ensure the machine safety, the highest applied depth of cut was $a_{\text{p}} = 16$ mm.

3.2 Input parameters for the stability investigations

For the calculation of the stability charts using the semi-discretization method, modal parameters and force coefficients are required beforehand. To determine the force coefficients, the process forces are measured experimentally with a Kistler 9257B three-component dynamometer. Thereafter, a particle swarm optimization algorithm is used to fit the measured process forces for one tool revolution with six cutting coefficients of a mathematical force model. Thereby, a trochoidal tooth path is assumed. The full algorithm is derived in [15]. The forces of the model can be calculated as follows, where F_{f}, F_{fN} and F_{p} are feed force, feed normal force and passive force, respectively:

$$\mathbf{\Phi}_{\exp,d}\langle T\rangle =$$

$$\Gamma_{j,u} \hat{=} [\Gamma_{d,j,u,2}\langle T,z_i\rangle \quad \Gamma_{d,j,u,1}\langle T,z_i\rangle]$$

EI/92696 © IFW

Fig. 5 Construction of the monodromy matrix. Thereby, the position of $\Gamma_{j,u}$ depends on the individual time delay [15]

prototype 1:	prototype 2:	roughing tool:	finishing tool:
$\Delta R = 20$ µm	$\Delta R = 40$ µm	$\Delta R = -$	$\Delta R = -$
$b_{\text{f}} = 200$ µm	$b_{\text{f}} = 200$ µm	$b_{\text{f}} = 200$ µm	$b_{\text{f}} = -$
$\alpha_{\text{f}} = 1°$	$\alpha_{\text{f}} = 1°$	$\alpha_{\text{f}} = 1°$	$\alpha_{\text{f}} = -$

EI/92697 © IFW

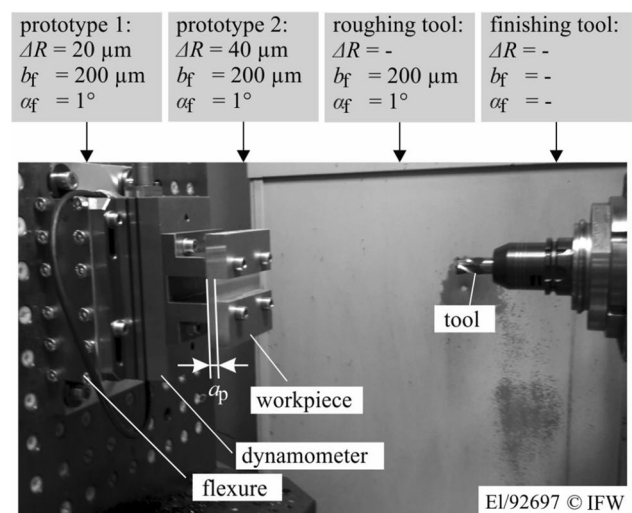**Fig. 6** Experimental setup and used tools. All tools possess four teeth, an unequal pitch angle $\Delta p = 10°$, a radius $R = 10$ mm and a helix angle $\delta = 30°$

$$\begin{bmatrix} F_r\langle t \rangle \\ F_{fN}\langle t \rangle \\ F_p\langle t \rangle \end{bmatrix} = \sum_{j=1}^{N_t} \sum_{i=1}^{N_z} \left[\mathbf{T}_j\langle t, z_i \rangle \sum_{u=1}^{N_t} \left[\begin{bmatrix} K_{tc} \\ K_{rc} \\ K_{ac} \end{bmatrix} h_{j,u}\langle t, z_i \rangle \right. \right.$$
$$\left. \left. + \begin{bmatrix} K_{te} \\ K_{re} \\ K_{ae} \end{bmatrix} \frac{1}{\sin(\kappa_j)\cos(\delta_j)} g_{j,u}\langle t, z_i \rangle z_d \right] \right]$$

with

$$\mathbf{T}_j\langle t, z_i \rangle = \begin{bmatrix} \cos(-\varphi_j) & -\sin(-\varphi_j)\sin(\kappa_j) & -\sin(-\varphi_j)\cos(\kappa_j) \\ \sin(-\varphi_j) & \cos(-\varphi_j)\sin(\kappa_j) & \cos(-\varphi_j)\cos(\kappa_j) \\ 0 & -\cos(\kappa_j) & \sin(\kappa_j) \end{bmatrix}$$
$$(22)$$

The curve fitting was carried out for the three tool concepts with the results shown in Fig. 7. The dashed lines picture the measured forces, the continuous lines show the calculated forces. Thereby, the specific cutting coefficients K_{tc}, K_{rc} and K_{ac} were set equal for all three tools based on the measurements of the finishing tool. This assumption is based on results of Sellmeier, who showed that the flank face chamfer only influences the edge coefficients K_{te}, K_{re} and K_{ae} [3]. The values shown are the mean value of ten fittings at different times of force measurement. The results show a good agreement between experimental and simulated process forces. The shape of the process forces of the prototype tool significantly differs from the process forces of the two other tools, which can be attributed to the radial recession of the chamfered cutting teeth. Additionally, higher maximum process forces can be observed for the roughing tool compared to the finishing tool, which is the result of an increased flank face to workpiece contact.

Furthermore, the process damping coefficient K_{pd} and the friction coefficient μ are needed to account for the influence of the flank face chamfer. The friction coefficient between the aluminium workpiece and the cemented carbide tool was assumed to be 0.3 based on [3, 15]. Since there are large differences between the process damping coefficients K_{pd} used in the literature, the calculations were carried out with two different coefficients $K_{pd} = 10{,}000$ N/mm^3 and $K_{pd} = 50{,}000$ N/mm^3. These values are in line with the ones used in [9, 15].

Frequency response functions (FRFs) were determined with an impact hammer test (hammer type PCB 086C03, aluminum tip). The output signals were measured with an accelerometer (type 352A21). Contactless measurements of the resulting displacement with a laservibrometer (Polytec OFV-3001) showed similar results. To reduce measurement errors, the FRFs were determined as means of ten impact tests. The modal parameters were determined using a genetic algorithm. The measured and fitted frequency response functions are shown in Fig. 8. The modal parameters are given in Tables 1, 2, 3 and 4. The system has the highest compliance in x-direction of the workpiece at 124 Hz due to the unidirectional flexure. The FRF of the
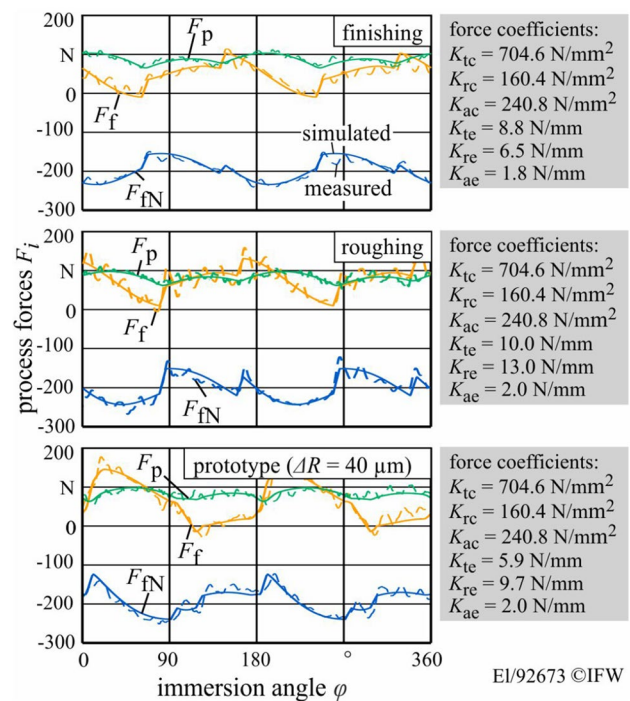
Fig. 7 Measured and simulated process forces for one tool revolution (feed per tooth $f_z = 0.12$ mm, depth of cut $a_p = 2$ mm, width of cut $a_e = 20$ mm, cutting speed $v_c = 251$ m/min, down milling)

workpiece in y-direction changes depending on the depth of cut a_p. However, calculated stability charts for the different FRFs indicate only a small influence of this mode on the process stability (Fig. 9). Therefore, only the FRFs for a depth of cut $a_p = 6$ mm were used for the calculation of the stability charts.

4 Results and discussion

Figure 10 shows the experimental and calculated stability charts of a roughing tool, a finishing tool and two prototype tools ($\Delta R = 40$ µm and 20 µm). The continuous lines illustrate the calculated stability charts, while the points of the experimental stability charts are marked with red (instable), yellow (marginal stable) and green (stable) symbols. The stability charts of the roughing tool and the prototype tools were calculated with process damping coefficients $K_{pd} = 10{,}000$ N/mm^3 (black lines) and $K_{pd} = 50{,}000$ N/mm^3 (grey lines).

In the upper diagramm, it can be seen that a good agreement exists between simulated and experimental stability charts for the sharp cutting tool. Possible deviations between calculated and experimental stability charts (e.g. at $n = 2000$ min^{-1}) could be caused by runout errors [15] or differences between real and modelled dynamic behaviour
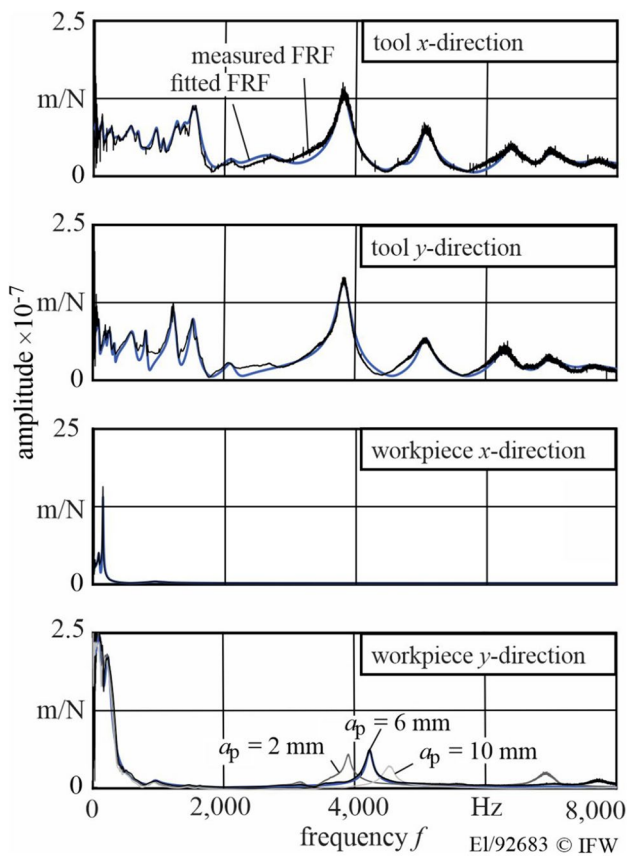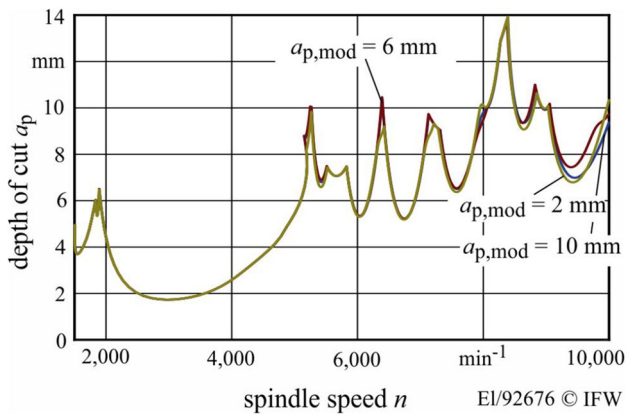
Fig. 8 Frequency response functions

Table 1 Modal parameters of the workpiece in *x*-direction

No.	*f* in Hz	*m* in kg	*d* in Ns/m	*k* in N/μm	*ζ* in %
1	85	34.4	9248.2	9.8	25.2
2	124	19.2	1349.6	11.7	4.5
3	951	4.2	6533.4	149.7	13.0

Table 2 Modal parameters of the workpiece in *y*-direction ($a_{p,mod} = 6$ mm)

No.	*f* in Hz	*m* in kg	*d* in Ns/m	*k* in N/μm	*ζ* in %
1	110	17.2	9966.0	8.2	42.0
2	216	6.1	3920.2	11.3	23.5
3	920	23.1	20,027.6	771.8	7.5
4	4220	1.0	638.7	730.2	1.2

Table 3 Modal parameters of the tool in *x*-direction

No.	*f* in Hz	*m* in kg	*d* in Ns/m	*k* in N/μm	*ζ* in %
1	31	10,781.8	308,343.5	411.4	7.3
2	36	14,537.8	353,170.6	743.8	5.4
3	140	204.4	36,619.8	159.8	10.1
4	284	51.3	27,848.4	163.7	15.2
5	379	58.0	36,020.4	329.6	13.0
6	592	22.5	13,703.5	312.0	8.2
7	690	40.5	10,958.1	761.8	3.1
8	697	5.9	9865.9	112.8	19.2
9	976	8.5	3873.4	318.5	3.7
10	1074	20.8	6022.1	950.1	2.1
11	1290	7.7	3745.7	506.1	3.0
12	1403	3.9	3402.9	299.8	5.0
13	1556	0.9	1012.2	90.4	5.5
14	2120	3.9	5686.0	703.2	5.4
15	2751	0.5	2256.0	148.9	13.0
16	3829	0.2	339.1	136.0	3.0
17	4709	1.8	3244.3	1604.1	3.0
18	5079	0.3	438.7	349.9	2.0
19	6389	0.3	605.3	447.5	2.7
20	6970	0.5	863.1	701.4	2.7
21	7602	0.5	1758.6	1214.0	3.5

Fig. 9 Calculated stability charts for different preparation states (feed per tooth $f_z = 0.12$ mm, width of cut $a_e = 20$ mm, axial discretization steps $N_z = 20$ mm, discretization steps for one tool revolution $N_k = 720$ mm). Thereby, $a_{p,mod}$ stands for the thickness of the workpiece at the prepared position

[18]. However, the measured runout error is approximately 2 μm. The influence is therefore only small. The highest experimental stability limit could be achieved at spindle speed $n = 8000$ min^{-1} with $a_{p,lim} = 9$ mm, which is close to the highest calculated stability limit at $n = 8500$ min^{-1}. To investigate the calculation approach in more detail, simulations using various axial discretization steps N_z as well as angular discretization steps N_k (Fig. 11a) and different modal parameters and force coefficients (Fig. 11b) are carried out. For a small number of discretization steps, there are regocnizable differences between the stability charts. However, the charts calculated with $N_z = 20$, $N_k = 720$ and $N_z = 25$, $N_k = 900$ are almost identical. Thus, the stability

Table 4 Modal parameters of the tool in *y*-direction

No.	*f* in Hz	*m* in kg	*d* in Ns/m	*k* in N/µm	*ζ* in %
1	75	238.9	3,813,213.8	53.6	16.9
2	187	484.8	3,257,353.5	673.6	2.9
3	256	43.6	1,390,578.7	113.1	9.9
4	317	170.6	1,578,896.8	678.6	2.3
5	608	6.2	471,628.4	90.1	10.0
6	798	12.3	304,491.4	309.4	2.5
7	1229	2.3	133,518.6	139.7	3.7
8	1520	1.6	110,179.3	149.1	3.5
9	2106	3.4	337,665.4	603.8	3.7
10	3833	0.2	26,862.6	112.7	2.9
11	5075	0.3	48,639.3	352.5	2.2
12	6270	0.3	61,954.6	452.0	2.7
13	6967	0.3	86,097.9	698.0	2.7
14	7558	0.5	177,008.3	1200.9	3.5

limits converge for a high number of discretization steps. The influence of force coefficients K_{tc} and K_{rc} on the stability limit is pictured in Fig. 11b. A change in the force coefficients leads to a shift in the stability limit along the y-axis. There is no significant influence on the shape of the curve. Additionally, a stability chart in which the dominant mode of the workpiece in the x-direction ($f_{tl,x2} = 124$ Hz) was not taken into account was calculated. This leads to a significant higher stability limit and a change in the shape of the stability charts for $n = 2000$–5500 min^{-1}. Due to the unequal tooth pitch of the tool, the periodicity of the process equals two times the spindle speed n. Accordingly, the periodicity for spindle speeds $n = 2000$–5500 min^{-1} is located in a frequency range $f = 66.6$–183.3 Hz, which corresponds to the dominant mode $f_{tl,x2} = 124$ Hz. At spindle speeds $n > 5500$ min^{-1}, the mode is irrelevant and the stability limit is identical to the reference process.

The charts of the roughing tool show significant higher experimental and calculated stability limits compared to the finishing tool. For spindle speeds $n = 6000$–$10,000$ min^{-1} all stability experiments were stable up to the maximum

Fig. 10 Calculated stability charts for different preparation states (feed per tooth $f_z = 0.12$ mm, width of cut $a_e = 20$ mm, axial discretization steps $N_z = 20$, discretization steps for one tool revolution $N_k = 720$)

a variation of N_z and N_k

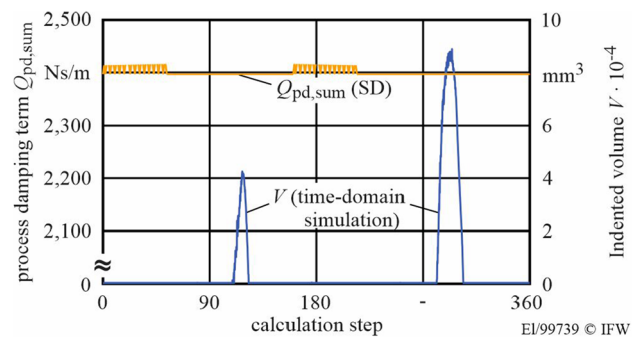**b** variation of K_{tc}, K_{rc} and modal parameters
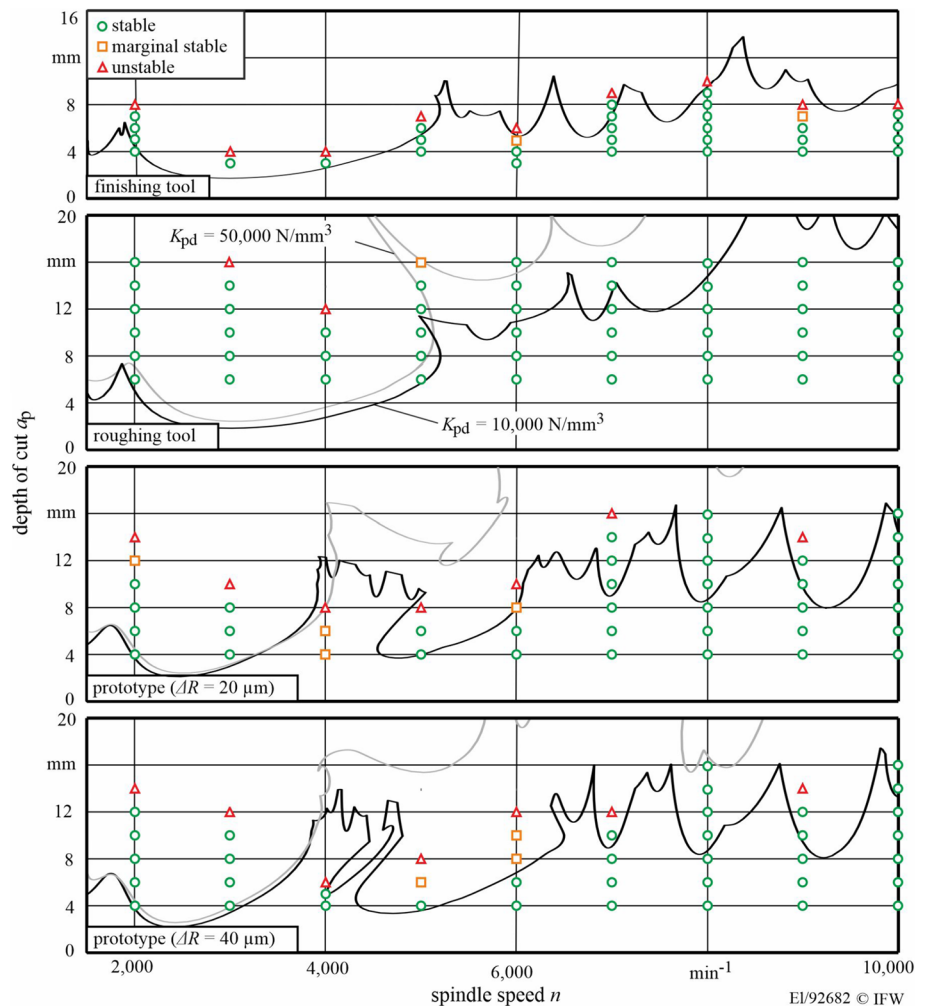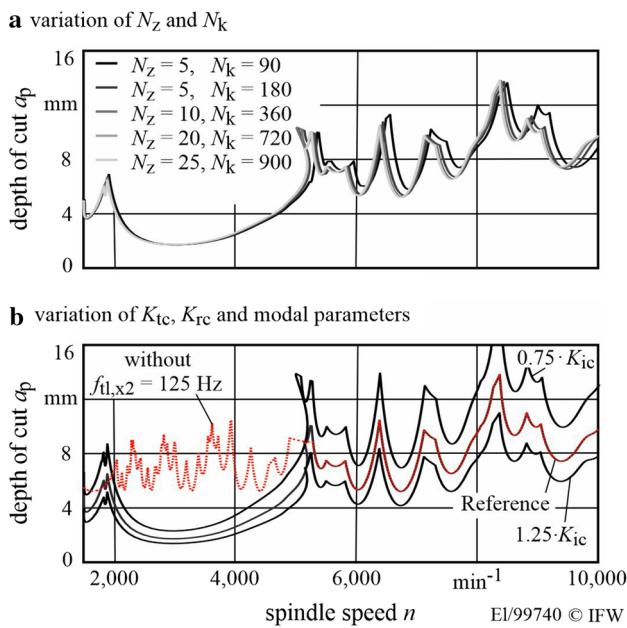
Fig. 11 Simulated stability charts of the finishing tool. **a** Variation of discretization steps N_z and N_k. **b** Variation of force coefficients and modal parameters for $N_z = 20$, $N_k = 720$

Fig. 12 Illustration of non-linear effects by comparing $Q_{pd,sum}$ with V calculated using time-domain simulations (feed per tooth $f_z = 0.12$ mm, width of cut $a_e = 20$ mm, depth of cut $a_p = 8$ mm, spindle speed $n = 9000$ min⁻¹, axial discretization steps $N_z = 20$, discretization steps for one tool revolution $N_k = 720$, $K_{pd} = 10,000$ N/mm³)

considered depth of cut $a_p = 16$ mm. Instable or marginal stable processes only appeared for spindle speeds $n = 3000$–5000 min⁻¹ with a minimum stability limit of $a_p = 10$ mm. For the calculated stability charts a low stability was determined for low spindle speeds $n = 2000$–5000 min⁻¹ similar to the calculated stability chart of the finishing tool. For $n > 6000$ min⁻¹ the roughing tool exhibits a significantly higher stability limit for both process damping coefficients K_{pd}. The increased calculated and experimental stability limits can be attributed to the process damping effect.

However, there are significant differences between calculated and experimental stability charts for the roughing tool. The deviations indicate inaccuracies in the process damping model. While some processes with low process damping effects can be modelled with sufficient accuracy as shown in [3, 10], the model does not seem to be applicable to the examined use cases. One possible explanation for this is the non-linear behaviour of the process damping. While the process damping force in the model is expressed as linear to the dynamic velocity over the entire system period, it only occurs in the real process if the tool moves into the workpiece and therefore actually indents material. To illustrate this effect, process damping considered in the semi-discretization is analyzed in more detail in Fig. 12. Figure 12 pictures the Frobenius norm of the process damping matrix

$$Q_{pd,sum}\langle t\rangle = \left\| \sum_{j,u=1}^{N_t} \sum_{i=1}^{N_z} Q_{j,u}\langle t, z_i\rangle \right\|_F, \quad (23)$$

which describes the overall acting tangential and radial process damping coefficient in x- and y-direction. The term is calculated for every calculation step of the semi-discretization and therefore one system period. In theory, process damping only occurs when material is indented by the flank face, which can be derived by the relative velocity between tool and workpiece as stated in [3]. However, the actual velocity vector can not be calculated with the semi-discretization since it simplifies the second-order linear delay differential equation to an eigenvalue problem. As a result, the process damping term is always added to the structural damping. The fluctuation of $Q_{pd,sum}$ can be attributed to numerical reasons. As comparison to the process damping term calculated with semi-discretization, the indented volume V, which is proportional to the process damping, was calculated using a time-domain simulation presented in [19] for one system period. It can be seen that the volume is zero for most of the discretization steps. Thus, time-domain simulations are a promising approach to improve the forecast accuracy as discussed in [15]. However, due to long calculation times, time-domain simulations can not create stability charts efficiently. Another approach to consider the non-linear behaviour in the semi-discretization is the linearization around the stationary solution of the dynamic milling system and therefore the prior calculation of the indented volume using the shooting method. However, this approach only works for systems with one single time-delay [20]. Further existing deviations between calculated and experimental stability charts could possibly be reduced by considering plastic deformations under the flank face and thermal effects.

The third diagram in Fig. 10 shows the experimental and calculated stability charts of the prototype with radial recession $\Delta R = 20$ µm. Compared to the finishing tool, the experimental stability limit increases significantly for most spindle speeds n (e.g. increased stability limit from $a_{p,lim} = 3$ mm to

$a_{\text{p,lim}} = 8$ mm at $n = 3000$ min^{-1}). This is the result of the process damping effect of the two chamfered cutting teeth. In comparison to the roughing tool, the experimental stability investigations indicate reduced process stability. This can be attributed to the fact that the process damping effect of the roughing tool is greater due to the four chamfered cutting edges. The calculated stability charts indicate a low stability limit for low spindle speeds n. By increasing the process damping coefficient K_{pd}, the stability limit increases significantly for spindle speeds $n > 4000$ min^{-1}. However, both stability charts do not fit with the experimental data, which is the result of inaccuracies in the modelling of the process damping effect.

The stability charts of the second prototype with radial recession $\Delta R = 40$ µm show similar results as the first prototype. The maximum deviation between the two experimental stability charts appears at spindle speed $n = 7000$ min^{-1}. The first prototype ($\Delta R = 20$ µm) is stable up to a depth of cut $a_{\text{p,lim}} = 14$ mm, while the second prototype ($\Delta R = 40$ µm) is stable up to a depth of cut $a_{\text{p,lim}} = 10$ mm. Furthermore, the calculated stability charts for $K_{\text{pd}} = 50{,}000$ N/mm^3 indicate a higher stability limit for $n = 4000$–6000 min^{-1} and a lower stability limit for $n > 6000$ min^{-1} compared to the first prototype tool. Experimental and calculated differences between the two prototypes can be attributed to two effects. First, a higher radial recession leads to a higher interruption of the regenerative effect and therefore an increasing stability limit [15]. Second, a higher radial recession leads to a later entry and earlier exit of the chamfered cutting teeth in the workpiece. Hence, the process damping is reduced.

In comparison of the four tools, the highest stability can be achieved with the roughing tool due to the highest process damping. In contrast to that, both prototype tools have a lower calculated and experimental stability limit for most spindle speeds n, since only two chamfered teeth contribute to the process damping. Nevertheless, for certain spindle speeds (e.g. $n = 4000$ min^{-1}) there are only slight differences between the stability limit of roughing-finishing-prototype and roughing tool. In addition to that, most industrial roughing processes do not work close to the stability limit. Therefore, there is a high potential in substituting conventional roughing tools with a roughing-finishing tool and thereby using only one tool for the machining process.

5 Conclusion and outlook

In this paper, process stability investigations for a novel roughing-finishing tool with two sharp and two chamfered radially recessed teeth as well as a conventional roughing tool (chamfered teeth only) and a conventional finishing tool (sharp teeth only) were conducted. An extended semi-discretization model was presented, applied for the different tool concepts and compared with experimental stability charts. A good agreement between calculated and experimental stability charts could be reached for the finishing tool. However, experimental and calculated stability charts of the prototype tools and the roughing tool show high deviations, which can be attributed to an inaccurate modelling of the process damping.

Calculated and experimental stability charts of the roughing-finishing prototypes show significantly increased stability limits up to 300% compared to the finishing tool. The process stability of a conventional roughing tool could not be reached for most spindle speeds n since the process damping effect is lower for the roughing-finishing prototype. Nevertheless, with the right chosen spindle speed n the differences between roughing tool and roughing-finishing prototype can be reduced. For example, the difference in stability limits between roughing tool and prototype ($\Delta R = 40$ µm) at a speed of $n = 3000$ min^{-1} is 10 mm, while the difference at a speed of $n = 5000$ min^{-1} is only 4 mm.

Further investigations will focus on the influence of manufacturing errors and wear on the tool concept. The control of the manufacturing process is important, since chamfer geometry and radial recession ΔR exhibit small dimensions and significantly influence process stability and surface quality. Wear investigations are of relevance due to a high flank wear on the chamfered cutting teeth. In addition, the roughing-finishing tool will be applied on different materials, e.g. steel and titanium. Moreover, the process damping model must be improved in order to increase the accuracy of the semi-discretization.

References

1. Hahn RS (1953) Metal-cutting chatter and its elimination. Trans ASME 78:1073–1080
2. Tobias SA, Fishwick W (1956) Eine Theorie des regenerativen Ratterns an Werkzeugmaschinen. Maschinenmarkt 17:15–30

3. Sellmeier V (2012) Über den Einfluss der Werkzeuggestalt auf die dynamische Stabilitt des Fräsprozesses. Leibniz Universität Hannover, PhD-Thesis

4. Munoa J, Beudaert X, Dombovari Z, Altintas Y, Budak E, Brecher C, Stepan G (2016) Chatter suppression techniques in metal cutting. CIRP Ann 65(2):785–808

5. Dombovari Z, Altintas Y, Stepan G (2010) The effect of serration on mechanics and stability of milling cutters. Int J Mach Tools Manuf 50:511–520

6. Dombovari Z, Stepan G (2012) The effect of helix angle variation on milling stability. J Manuf Sci Eng 134

7. Totis G, Albertelli P, Sortino M, Monno M (2014) Efficient evaluation of process stability in milling with spindle speed variation by using the chebyshev collocation method. J Sound Vib 333:646–668

8. Wu D (1988) Comprehensive dynamic cutting forces model and its application to wave-removing processes. ASME J Eng Ind 110:153–61

9. Sellmeier V, Denkena B (2012) High speed process damping in milling. CIRP J Manuf Sci Technol 5:8–19

10. Budak E, Tunc LT (2010) Identification and modelling of process damping in turning and milling using a new approach. CIRP Ann 59:403–408

11. Chiou RY, Liang SY (1998) Chatter stability of a slender cutting tool in turning with tool wear effect. Int J Mach Tools Manuf 38(4):315–327

12. Jin X, Alitntas Y (2013) Chatter stability model of micro-milling with process damping. J Manuf Sci Eng 135

13. Ahmadi K, Ismail F (2012) Stability lobes in milling including process damping and utilizing multi-frequency and semi-discretization methods. Int J Mach Tools Manuf 54–55:46–54

14. Jing LL, An LQ, Chen M (2008) Study on Burr formation in face milling of stainless steel with chamfered cutting tool. Adv Mater Res 53–54:83–88

15. Grabowski R (2019) Enhanced simulation of the milling process for a novel roughing and finishing tool. Leibniz Universität Hannover, PhD-Thesis

16. Denkena B, Köhler J, Grabowski R (2013) Konzept eines Fräswerkzeugs für die Schrupp- und Schlichtbearbeitung. DE102013225017.7

17. Denkena B, Grove T, Ellersiek L (2018) A novel tool concept for roughing and finishing operations. Proc Manuf 18:27–34

18. Postel M, Bugdayci NB, Monnin J, Kuster F, Wegener K (2018) Improved stability predictions in milling through more realistic load conditions. Proc CIRP 77:102–105

19. Denkena B, Grove T, Pape O (2019) Optimization of complex cutting tools using a multi-dexel based material removal simulation. In: 17th CIRP conference on modelling of machining operations

20. Bachrathy D, Stepan G (2010) Time-periodic velocity-dependent process damping in milling processes. In: 2nd CIRP international conference on process machine interactions